International Journal of Minerals, Metallurgy and Materials
Accepted manuscript, https://doi.org/10.1007/s12613-025-3087-9

Sodium storage properties of Fe, Ni-bimetallic doped carbon-modified $NaTi_2(PO_4)_3$

Junling Che[1)], *Jiaojiao Yu*[1)], *Tong Xu*[1,2),✉], *Junchao Ma*[1)], *Kang Yu*[2)], *Jian Qin*[2)], *Wei Ren*[1)], *Yanmin Jia*[3),✉], *and Xifei Li*[2),✉]

1) School of Science, Xi'an University of Posts and Telecommunications, Xi'an 710121, China

2) Institute of Advanced Electrochemical Energy, School of Materials Science and Engineering, Xi'an University of Technology, Xi'an 710048, China

3) School of Physics and Information Technology, shaanxi Normal University, Xi'an 710062, China

✉Corresponding authors: Tong Xu E-mail: xutong911@xupt.edu.cn; Yanmin Jia E-mail: ymjia@snnu.edu.cn; Xifei Li E-mail: xfli@xaut.edu.cn

Abstract: $NaTi_2(PO_4)_3$ (NTP) is a material with a NASICON structure, a three-dimensional open type skeleton, and suitable negative voltage window, which is widely regarded as a magnetic anode material for aqueous sodium ion batteries (ASIBs). However, NTP's intrinsically poor conductivity hampers their use in ASIBs. Herein, bimetallic doped carbon material was designed and combined with the sol-gel method to prepare $NaTi_2(PO_4)_3$-C-FeNi (NTP-C-FeNi) composite materials. This bimetallic doped carbon composite NTP material not only has a large specific surface area, but also effectively improves conductivity and promotes rapid migration of Na^+. Following the rate performance test, NTP-C-FeNi retained a reversible capacity of 116.75 $mAh \cdot g^{-1}$ at 0.1 $A \cdot g^{-1}$, representing 95.9% of the first cycle capacity. After 500 cycles at 1.5 $A \cdot g^{-1}$, the cycle fixity was 85.3%. The enhancement of electrochemical performance may owe to the widening of pathways and acceleration of Na^+ insertion/extraction facilitated by FeNi-C doping, while the carbon coating effectively promotes electrode charge transfer. The results indicate that the bimetallic doped carbon composite $NaTi_2(PO_4)_3$ holds potential for practical applications in novel aqueous sodium ion battery systems.

Keywords: aqueous sodium-ion batteries; $NaTi_2(PO_4)_3$; bimetallic doped carbon; electrochemical performance

1. Introduction

Battery technology is considered a reliable means for efficiently storing both conventional and renewable energy. Although lithium-ion batteries (LIBs) continue to dominate the market, it is anticipated that multiple battery types will coexist in the future [1-4]. Aqueous batteries are increasingly gaining attention due to their low cost, high safety, and environmental friendliness [5, 6]. However, the consumption of lithium resources may lead to supply shortages [7, 8]. As a result, ASIBs, which are characterized by widespread resource availability, low production cost, and reduced environmental impact, are expected to emerge as a promising alternative to LIBs [9-11].

As the core component of batteries, the development of stable and reliable electrode materials has become a top priority [12]. $NaTi_2(PO_4)_3$ is characterized by a three-dimensional structure, enabling the reversible insertion and extraction of sodium ions, facilitating the reversible transformation between $NaTi_2(PO_4)_3$ and $Na_3Ti_2(PO_4)_3$ [13]. Additionally, aqueous electrolytes are demonstrated to exhibit better conductivity, lower viscosity, and superior sodium ion transfer kinetics compared to non-aqueous electrolytes, outperforming lithium-ion secondary batteries in these aspects [14]. Nevertheless, owing to the isolated TiO_6 octahedra within the NTP structure, the material exhibits poor electronic conductivity and suboptimal electrochemical performance in its pure phase.

In view of this, pure-phase NTP has been successively modified by researchers to improve its electrochemical performance. The general modifications include coating [15-17], structure optimization [18-20], and doping [21-23]. The performance of NTP materials can be improved through coating, resulting in higher energy density and longer cycle life. As reported by Xu et al. [24], carbon-coated porous NTP nanorods have been shown to significantly improve long-cycle performance. Furthermore, the optimization of the nanostructure provides nanoscale channels for

sodium ions, and the large contact area between the electrolyte and the electrode facilitates enhanced electrochemical performance [25]. Additionally, the small particle size of NTP shortens the diffusion paths of Na^+ and enhances the insertion and extraction of Na^+, thereby improving the electrochemical performance of the electrodes. Wu et al. [26] designed, for the first time, a micro-sized 3D graphene network embedded with nanoscale porous NASICON-type NTP particles, which retained 80% of its initial charge capacity after 1000 cycles at 10 C. Doping of NTP can be divided into body doping and carbon layer doping. Doping the Ti sites in NTP with metal cations [27, 28] can enlarge the size of the cell while keeping the original crystal structure unaffected, thereby providing a larger sodium ion transport channel and a larger intercalation space. For instance, Siham et al. [29] reported $Na_{1.5}Fe_{0.5}Ti_{1.5}(PO_4)_3$/C used in SIB, demonstrating that Fe replaced Ti and carbon coatings, respectively, enhancing ionic and electronic conductivity and improving electrochemical performance. Similarly, Mn-based NTP materials were prepared by Wu et al. [30] for aqueous sodium-ion systems, demonstrating good electrochemical performance and suitable working potential. Doping at the Na site and $(PO4)_3^-$ site of NTP has been shown it can also improve the electrochemical performance [31, 32]. Wang et al. [33] introduced oxygen vacancies (Vo) into a core-shell C@$NaTi_2(PO_4)_3$-x composite to improve cycle stability, with C@$NaTi_2(PO_4)_3$-1.0 composites demonstrating the most stable cycle performance and best rate performance. Doping of carbon layer materials with anions such as F, S, and N has also been employed to enhance NTP electrochemical performance [34, 35]. Although coating, structural optimization, and doping have significantly improved the performance of NTP materials, few studies have proposed metal cation doped carbon layer modified NTP composites.

In this paper, the design of Fe and Ni bimetallic doped carbon materials has been optimized. For the first time, NTP was combined with Fe-C, Ni-C, and FeNi-C materials using the sol-gel method to form carbon-coated NTP composite materials loaded on a carbon matrix. The resulting $NaTi_2(PO_4)_3$-C-FeNi (NTP-C-FeNi) composite electrode demonstrated excellent electrochemical performance, with a rate

capability of 95.9% at 0.1 $A \cdot g^{-1}$ and cycle stability of 85.3% of the initial capacity after 500 cycles at 1.5 $A \cdot g^{-1}$. Additionally, the dynamic intercalation mechanism of Na^+ was investigated in depth, and it was found that the sodium ion diffusion rate was significantly improved. This promising design has been shown to optimize the microstructure of NTP composites, improve electronic conductivity, and enhance the Na^+ diffusion coefficient, thereby providing a novel approach for the modification and development of NTP negative electrodes and related electrode materials.

2. Experimental

The synthesis process of bimetallic doped carbon materials (FeNi-C) was carried out as follows: Firstly, 30 g of NaCl was used as a template, ammonium citrate ($C_6H_{17}O_7N_3$, 4.28 g) as a carbon source, melamine (0.68 g) as a nitrogen source, and iron acetylacetonate (0.07 g) and nickel acetylacetonate (0.05 g) as metal sources. These components were co-dissolved in deionized water, and the homogeneous solution was obtained by stirring thoroughly for 12 hours. The solution was then placed in a refrigerator and frozen to ensure it was completely solidified into ice. Next, freeze-drying was performed, during which NaCl crystallized to form regular nanocrystal arrays, resulting in the formation of precursors. During this process, the carbon, nitrogen, and metal sources were uniformly dispersed within the NaCl template. The precursor was then placed in a tube furnace and held at 1000°C for 2 hours under a nitrogen atmosphere. Under these conditions, the metal grew into carbon flakes, protected by the NaCl template within the restricted domain. Finally, the NaCl template was removed by repeated washing with deionized water, resulting in the FeNi-doped carbon material, designated as FeNi-C. Using the same method, two other metal-doped carbon materials were prepared, named Fe-C and Ni-C.

The synthesis of $NaTi_2(PO_4)_3$-C-Fe, $NaTi_2(PO_4)_3$-C-Ni, and $NaTi_2(PO_4)_3$-C-FeNi was carried out as follows: 1.7 ml of butyl titanate was dissolved in 20 mL of anhydrous ethanol in a three-necked flask. Then, added 0.208 g of anhydrous sodium acetate, 0.5 g of citric acid, and 0.03 g of the prepared Fe-C, Ni-C, and FeNi-C materials. The mixture was heated at 50°C with constant stirring for 0.5 hours to

ensure even and complete dissolution. Separately, 0.515 ml of phosphoric acid was added to 18 ml of anhydrous ethanol, and the solution was ultrasonically vibrated for 20 minutes at room temperature to achieve a homogeneous mixture. This phosphoric acid solution was then added dropwise to the three-necked flask at intervals of 0.5 hours. The reaction mixture was covered and allowed to react fully at 50°C for 3 hours. Finally, the temperature was increased to 80°C, and the fan was set to 30 until the $NaTi_2(PO_4)_3$-C-Fe, $NaTi_2(PO_4)_3$-C-Ni, and $NaTi_2(PO_4)_3$-C-FeNi precursor powders were obtained. The precursor powders were then placed in a tube furnace and calcined at 700°C for 5 hours in an argon atmosphere. The resulting composites were designated as NTP-C-Fe, NTP-C-Ni, and NTP-C-FeNi, respectively. The elemental weight percentages and atomic percentages of NTP-C-FeNi material are detailed in Table S1. Specifically, the weight percentages of C, O, Na, P, Ti, Fe, and Ni are 20.46%, 40.92%, 7.95%, 12.19%, 14.75%, 2.04%, and 1.69%, respectively, while the atomic percentages are 31.7%, 47.59%, 6.44%, 7.32%, 5.73%, 0.69%, and 0.54%, respectively.

3. Material characterization

X-ray diffractometer (XRD) of NTP-C-Fe, NTP-C-Ni, and NTP-C-FeNi were collected using D/Max2550VB+/PC within the 2θ range of 10°-80°. The microstructure of the composites was characterized by a JEOL JSM-7000F field emission scanning electron microscope (SEM) and a JEOL JEM-2100 transmission electron microscope (TEM). Raman spectra were obtained using a Horiba Lab RAM HR Evolution instrument. X-ray photoelectron spectroscopy (XPS) data were collected on a Thermo Scientific K-Alpha. The specific surface area and pore size distribution were measured using a Micromeritics ASAP 2460 automatic specific surface and porosity analyzer. Thermogravimetric analysis (TGA) data were acquired using the STA 449 F3 instrument.

4. Electrochemical measurements

To evaluate the rate performance, reversibility performance, and cycling

performance of NTP-C-Fe, NTP-C-Ni, and NTP-C-FeNi, the prepared composite active material, acetylene black, and PVDF were mixed in a ratio of 8:1:1. PVDF was first dissolved in NMP to form a uniform mixture, after which the active material and acetylene black were added with stirring. The resulting mixture was then coated onto nickel mesh that had been pre-washed, dried, and weighed. The coated nickel mesh was placed in a vacuum drying oven and maintained at 100°C for 10 hours. The mass after drying was recorded for parameter calculations in the battery tests.

A three-electrode test system was adopted to assemble half-cells, using a platinum sheet as the counter electrode, a saturated calomel electrode as the reference electrode, 5 mol $NaNO_3$ as the electrolyte, and prepared composite as the working electrode. The rate performance and cycle stability of the assembled cells were evaluated using a SLAN-CT2001A. Cyclic voltammetry curves were tested at scan rates of 0.2, 0.5, 1, 2, 5, and 10 $mV \cdot s^{-1}$ using a CHI760E electrochemical workstation. The electrochemical impedance spectra were measured in the frequency range of 10^6 to 0.01 Hz.

5. Results and Discussion

5.1. Characterization of NTP composites

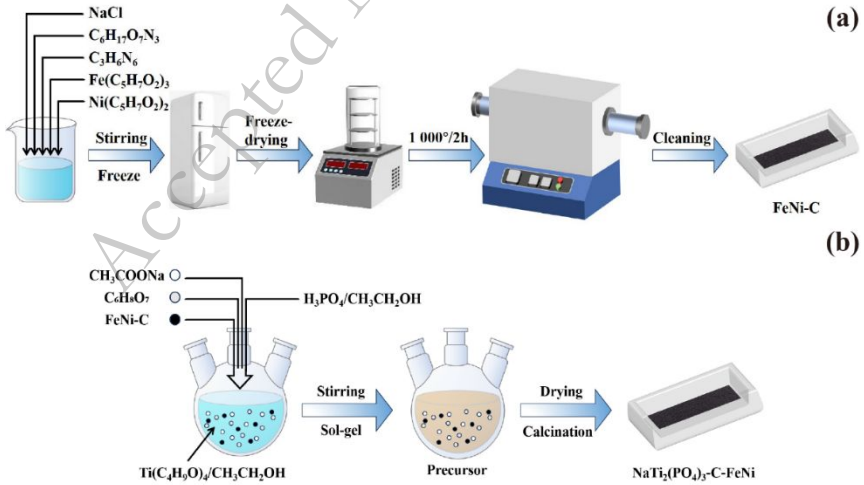

Fig. 1. Schematic illustration of the preparation process (a) bimetallic doped carbon material (FeNi-C); (b) $NaTi_2(PO_4)_3$-C-FeNi material.

A schematic illustration of the preparation process is shown in Fig. 1. Fig. 1(a)

illustrates the key steps in the synthesis of FeNi-C, including the freezing of the homogeneous solution, drying, heating under a nitrogen atmosphere and subsequent washing. Since the focus of this study is on the performance of the bimetallic-doped carbon when composite with NTP, an in-depth discussion of the bimetallic-doped carbon itself is not provided. However, relevant references can be consulted for further details [36-39]. Fig. 1(b) shows the main process of the composite of FeNi-C and NTP through the sol-gel method.

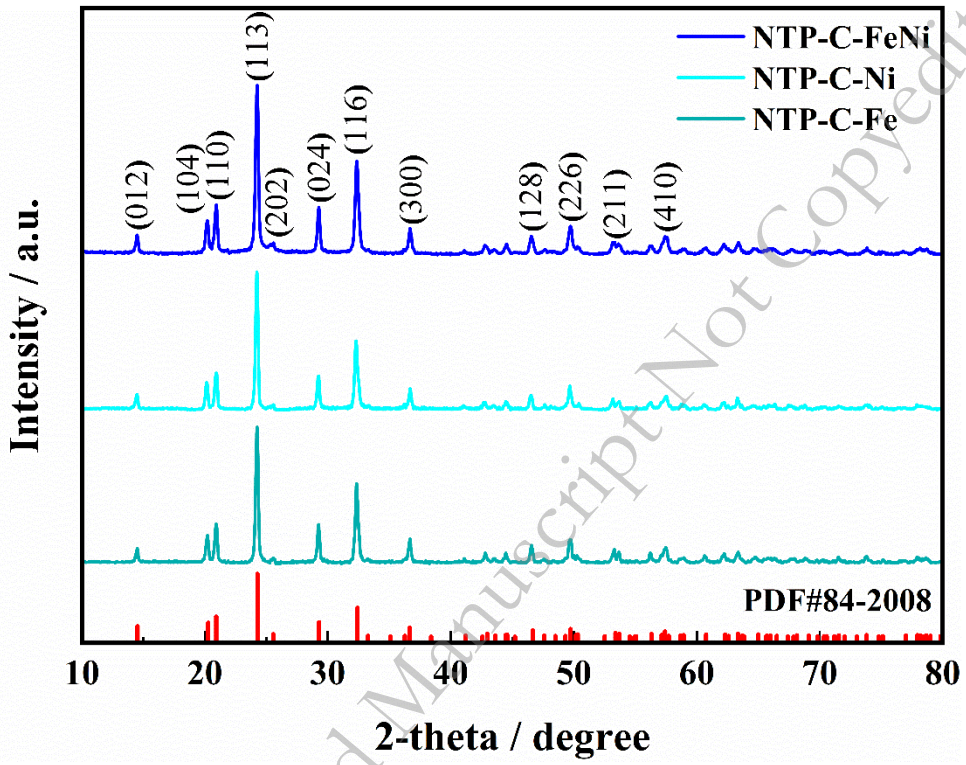

Fig. 2. XRD patterns of NTP-C-Fe, NTP-C-Ni and NTP-C-FeNi composite electrode materials.

The precise phase information of the NTP-C-Fe, NTP-C-Ni, and NTP-C-FeNi samples was obtained using XRD (Fig. 2). These three composite materials have diffraction peaks with strong peak intensities. The typical characteristic peaks align precisely with those of the reference card (PDF#84-2008). By observing and analyzing the XRD patterns of the three composites, it was found that the positions corresponding to the diffraction peaks of the composite electrode materials did not shift after carbon coating and doping. This indicates that the modification did not disrupt the lattice structure of the materials, and that the calcined NTP-C-Fe, NTP-C-

Ni, and NTP-C-FeNi materials maintained good crystallinity.

The surface microstructure of the NTP-C-FeNi material in Fig. 3(a) exhibits that it has a relatively homogeneous dispersion state. Compared with NTP-C-Fe (Figs. S1(a)-(b)) and NTP-C-Ni (Figs. S1(c)-(d)), there is minimal adhesion or agglomeration, and the surface profile is clear, reaching a nanometer scale. The high-magnification SEM image of NTP-C-FeNi material in Fig. 3(b) reveals a uniform microporous structure with evenly distributed pores, as indicated by the yellow-marked regions. This suggests that NTP-C-FeNi exhibits good dispersion and microporosity, which facilitates the rapid removal of Na^+ and enhances electron transport. Figs. 3(c)-(e) illustrate that all three samples exhibit a network porous morphology. The larger particles, labeled in the images, correspond to NTP, while the smaller particles represent FeNi metal. The metal nanoparticles are attached to the carbon matrix, and this morphology is consistent with previously reported bimetallic-doped carbon materials [37]. However, the carbon matrix in NTP-C-Fe (Fig. 3(c)) and NTP-C-Ni (Fig. 3(d)) is unevenly distributed, showing noticeable agglomeration. TEM and HRTEM images in Fig. 3(e) and Fig. 3(f) demonstrate that the NTP-C-FeNi nanoparticles possess an internal porous structure, with the carbon matrix uniformly dispersed. The NTP particles are coated with carbon and loaded onto the carbon matrix. The crystal plane spacing is measured to be 0.348 nm, corresponding to the (113) crystal plane of NTP.

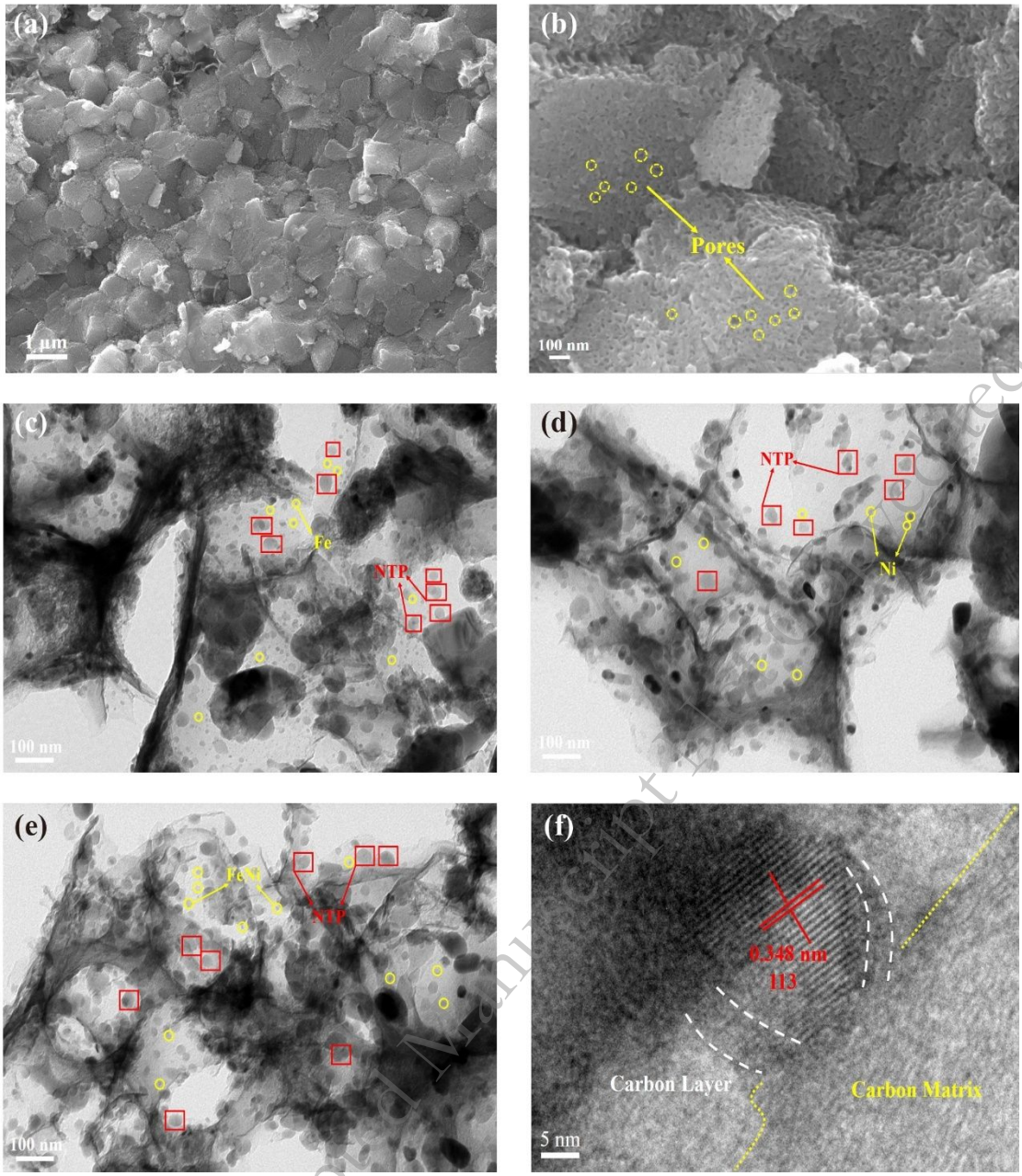

Fig. 3. Microscopic morphologies of three composites: (a) (b) SEM of NTP-C-FeNi; (c) TEM of NTP-C-Fe; (d) TEM of NTP-C-Ni; (e) (f) TEM and HRTEM of NTP-C-FeNi.

The Raman test results of NTP-C-Fe, NTP-C-Ni, and NTP-C-FeNi are depicted in Fig. 4(a). Distinct D and G band peaks are observed near 1340 and 1585 cm^{-1}. The relative strengths between the D and G bands are typically used to assess the integrity and degree of graphitization of carbon materials [40]. Highly graphitized carbon indicates good electronic conductivity, facilitating the separation and transfer of electrons. Conversely, the presence of defects in the carbon can alter the electronic

structure and optimize the adsorption energy of reacting molecules. The calculated I_D/I_G ratio (0.91) of the NTP-C-FeNi composite is lower than that of NTP-C-Fe (1.02) and NTP-C-Ni (0.99), indicating that NTP-C-FeNi possesses a highly ordered carbon structure with fewer defects, resulting in high electronic conductivity and significant enhancement of multiplicative properties. The thermogravimetric curves of NTP-C-FeNi, NTP-C-Fe, NTP-C-Ni, and NTP-C samples are illustrated in Fig. 4(b) and Figs. S2(a), S3(a), and S4(a), respectively. Four samples were heated from 30 °C to 800 °C in an oxygen environment, and the curves of mass variation with temperature were obtained. The NTP-C-FeNi sample showed quality loss starting from 100 °C, which may be caused by residual ethanol and water during the preparation process. Subsequently, a significant decrease in mass is observed in the range of 400 to 550 °C. According to the report [41], the pure NTP materials remain steady in this range. Therefore, the loss of mass is due to the surface carbon layer concent , which was calculated to be 3.93%.. The carbon content of NTP-C-Fe, NTP-C-Ni, and NTP-C samples is calculated to be 4.13%, 3.77%, and 2.24%, respectively. Fig. 4(c) shows the N_2 adsorption/desorption isotherms of the NTP-C-FeNi sample, indicating the type IV adsorption-desorption isotherm, suggesting a mesoporous structure. The specific surface area of NTP-C-FeNi material is 56.56 $m^2 \cdot g^{-1}$, and the average pore diameter is in the range of 3-15 nm, which is consistent with observations from HRTEM. This pore structure with a very big specific surface area facilitates the fast migration of Na^+ between the electrolyte and the NTP-C-FeNi anode material [42]. Additionally, the stability properties of NTP-C-FeNi aids in mitigating volume changes and irreversible phase transitions induced by repeated sodium ion intercalation. Furthermore, the N_2 adsorption and desorption isotherms of NTP-C-Fe, NTP-C-Ni, and NTP-C samples are presented in Figs. S2(b), S3(b), and S4(b), respectively. The results reveal a specific surface area of 8.60 $m^2 \cdot g^{-1}$ for NTP-C-Fe and 19.43 $m^2 \cdot g^{-1}$ for NTP-C-Ni, with average pore sizes falling within the range of 4-12 nm and 3-11 nm, respectively. Besides, NTP-C exhibits a specific surface area of 4.30 $m^2 \cdot g^{-1}$, with an average pore size ranging from 4-10 nm. To understand the valence states of each element on the surface of the composites, XPS spectra of NTP-

C-Fe, NTP-C-Ni, and NTP-C-FeNi materials were analyzed. The results demonstrate that all three composite surfaces contain C, O, P, Ti, and Na, with iron present in NTP-C-Fe (Fig. S2(c)), nickel in NTP-C-Ni (Fig. S3(c)), and both iron and nickel in NTP-C-FeNi (Fig. 4(d)). In addition, as shown in Fig. 4(e), the C1s spectrum of NTP-C-FeNi reveals peaks at 284.8, 286.38, 287.68, and 289.7 eV, corresponding to C-C, C-O, C=C, and O-C=O bonds, respectively. In the Ti 2p spectrum (Fig. 4(f)), the two main peaks at 460.3 eV and 466.0 eV are attributed to the $2p_{3/2}$ and $2p_{1/2}$ of Ti^{4+}, while the peaks at 459.1 eV and 463.1 eV correspond to the lower oxidation state of Ti^{3+}, indicating primarily a +4-valence state for Ti. The peaks at 711.8 eV and 728.1 eV correspond to the $Fe2p_{3/2}$ and $Fe2p_{1/2}$ orbitals of Fe^{3+}, while those at 710.7 eV and 727.0 eV correspond to $Fe2p_{3/2}$ and $Fe2p_{1/2}$ orbitals of Fe^{2+}, respectively. Additionally, three peaks at 713.6 eV, 717.3 eV, and 731.3 eV are assigned to satellite peaks (Fig. 4(g)). In Fig. 4(h), peaks at 854.5 eV and 872.6 eV correspond to the Ni $2p_{3/2}$ and Ni $2p_{1/2}$ orbitals of Ni^{2+}, while peaks at 857.8 eV and 876.8 eV correspond to Ni $2p_{3/2}$ and Ni $2p_{1/2}$ orbitals of Ni^{3+}.

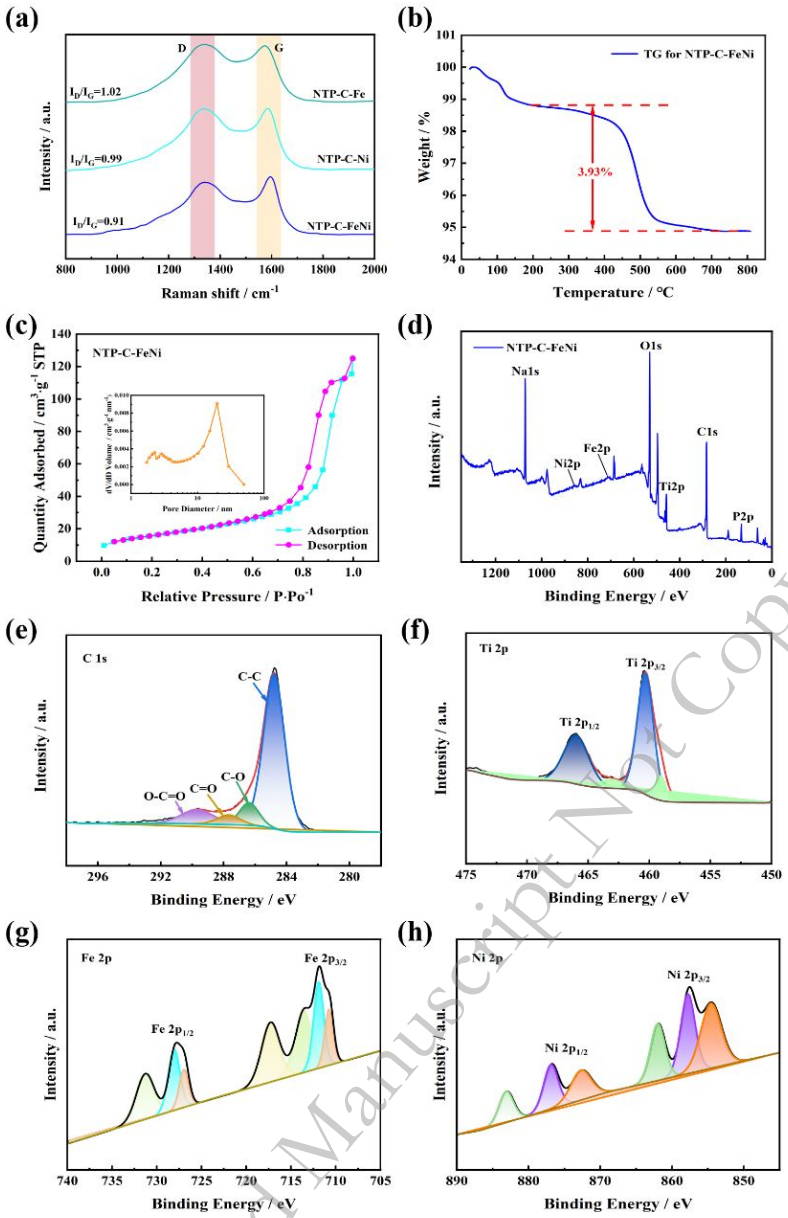

Fig. 4. (a) Raman of NTP-C-Fe, NTP-C-Ni and NTP-C-FeNi composites; (b) TG analysis for NTP-C-FeNi ; (c) N_2 adsorption-desorption isothermal curves and pore size distributions for NTP-C-FeNi ; (d) XPS spectrum for NTP-C-FeNi; (e)-(h) The elemental XPS spectrum of C, Ti, Fe and Ni.

5.2. Electrochemical performance testing

To rapidly obtain the electrochemical reaction information of NTP-C-Fe, NTP-C-Ni, NTP-C-FeNi, and NTP-C composite electrodes, the CV curves of these four composite electrode materials were compared under the same conditions: a scan rate of 2 mV/s, using a platinum counter electrode, a saturated calomel reference

electrode, and a 5 M $NaNO_3$ aqueous solution as the electrolyte in a three-electrode system, as depicted in Fig. 5. The CV curves of the four composite materials exhibit two changes corresponding to the peak current and the increase in overpotential of the oxidation-reduction peaks. Moreover, the potentials corresponding to the oxidation-reduction peaks of the four composite electrode materials show minimal differences under the same sweeping speed (NTP-C-Fe: -0.921/-0.699; NTP-C-Ni: -0.935/-0.721; NTP-C FeNi: -0.917/-0.731; NTP-C: -0.947/-0.693). However, the peak current densities and peak areas of the NTP-C-FeNi material are larger, indicating better reactivity and higher specific capacity of the electrode. This could be attributed to the fact that the large specific surface area by FeNi-C doping at the same dosage substantially improving the electrode/electrolyte contact and resulting in enhanced electrochemical performance of the FeNi-C doped $NaTi_2(PO_4)_3$ composite material.

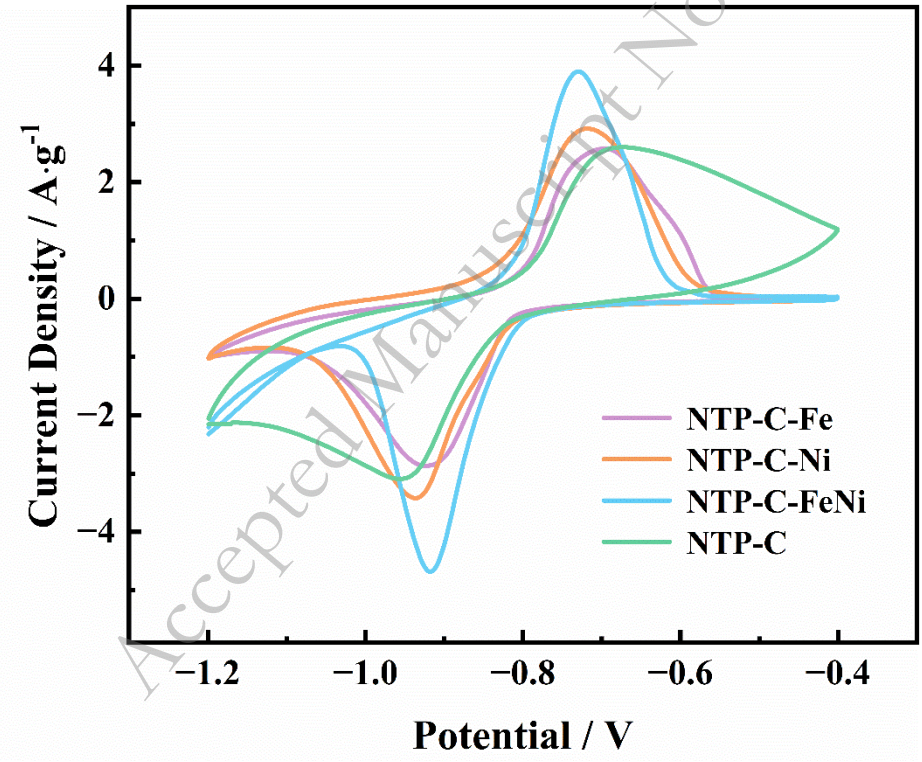

Fig. 5. CV curves of NTP-C-Fe, NTP-C-Ni, NTP-C-FeNi and NTP-C at 2mV·s^{-1}.

To further elucidate the enhancement of NTP's electrochemical performance by FeNi-C, constant current charge-discharge tests were conducted. The cycling performance of the NTP-C-Fe, NTP-C-Ni, NTP-C-FeNi, and NTP-C composite electrode materials was compared at 0.1 A·g^{-1}, as shown in Fig. 6(a). The results of

the cycling test at 0.1 $A \cdot g^{-1}$ indicated that the NTP-C-FeNi electrode maintained a relatively high capacity after 100 cycles, which is superior to that of NTP-C-Fe, NTP-C-Ni and NTP-C, at which time the NTP-C only provided 60.1 $mAh \cdot g^{-1}$. The rapid capacity decay of NTP-C may be attributed to parasitic redox reactions [43]. Additionally, Fig. 6(b) depicts the capacity-voltage curves of the NTP-C-FeNi electrode at different cycles under 0.1 $A \cdot g^{-1}$, which align with the CV curves and demonstrate good electrochemical response repeatability. The rate performance of NTP-C-Fe, NTP-C-Ni, NTP-C-FeNi, and NTP-C was compared in Fig. 6(c). The initial discharge capacities of the NTP-C-Fe composite electrode materials were 120.63, 106.96, 81.78, 65.89, and 50.17 $mAh \cdot g^{-1}$ at 0.1, 0.2, 0.5, 1, and 3 $A \cdot g^{-1}$, respectively. After charging and discharging tests under different rates and returning to a small current density of 0.1 $A \cdot g^{-1}$, NTP-C-Fe still exhibited a reversible capacity of 104.46 $mAh \cdot g^{-1}$, which is 86.5% of the first cycle capacity in the electrochemical test. Similarly, the first cycle discharge capacities of the NTP-C-Ni composite electrode material were 116.67, 106.61, 88.05, 79.59, and 71.87 $mAh \cdot g^{-1}$, respectively. After returning to a small current density of 0.1 $A \cdot g^{-1}$, NTP-C-Ni still demonstrated a reversible capacity of 111.41 $mAh \cdot g^{-1}$, which is 95.4% of the capacity of the first cycle in the electrochemical test. When tested at 0.1, 0.2, 0.5, 1, and 3 $A \cdot g^{-1}$, the first cycle discharge capacities of NTP-C-FeNi composite electrode materials were 121.72, 110.42, 97.71, 92.08, and 87.29 $mAh \cdot g^{-1}$, respectively. After charge and discharge tests at different rates and returning to a low current density of 0.1 $A \cdot g^{-1}$, NTP-C-FeNi still retained a reversible capacity of 116.75 $mAh \cdot g^{-1}$, which is 95.9% of the capacity of the first loop of the electrochemical test. Furthermore, NTP-C under the same test conditions exhibited first cycle capacities of 106.16, 87.83, 78.33, 69.16, and 57.5 $mAh \cdot g^{-1}$. After returning to a low current density, a capacity of 87.83 $mAh \cdot g^{-1}$ was retained, which is 82.7% of the first cycle capacity in the electrochemical test. This result clearly shows that NTP-C-FeNi exhibits superior electrochemical rate performance. In Fig. 6(d), the first cycle charge and discharge curves of the four materials at 0.1 $A \cdot g^{-1}$ are displayed. Stable charge and discharge plateaus are observed in the charge-discharge curves of all four materials. However, a

smaller potential difference ΔE is noted for the NTP-C-FeNi material, indicating lower polarization. As shown in Fig. 6(e), NTP-C-FeNi exhibits durable cycling capability at high current densities. At 1.5 $A \cdot g^{-1}$, the first cycle discharge capacities of NTP-C-Fe, NTP-C-Ni, NTP-C-FeNi, and NTP-C are 121.52, 119.06, 122.13, and 114.95 $mAh \cdot g^{-1}$, respectively. After 500 cycles, the capacity retention rates for NTP-C-Fe, NTP-C-Ni, NTP-C-FeNi, and NTP-C are 68.2%, 56.4%, 85.3%, and 47.7%, respectively. These results indicate that FeNi-C significantly enhances the sodium ion diffusion kinetics, leading to the superior cycling stability and prolonged lifespan of NTP-C-FeNi. Additionally, uniform carbon doping is beneficial for improving the electronic conductivity of the anode material. Fig. 6(f) displays the charge and discharge curves of the four materials after 500 cycles at 1.5 $A \cdot g^{-1}$. It is evident that, after cycling, the NTP-C-FeNi material still exhibits the lowest polarization, a result corroborated by the CV curves obtained at the same scan rate. These findings indicate that FeNi-C doping enhances the electrochemical performance of NTP. This improvement is attributed to its high specific surface area and porous structure, which contributes to the fast migration of Na^+ within the electrolyte and electrode material. The reaction equations for the NTP-C-FeNi composites during charging and discharging are given below:

Charge reaction equation

$$NaTi_2(PO_4)_3 + 2Na^+ + 2e^- \rightarrow Na_3Ti_2(PO_4)_3$$

Discharge reaction equation

$$Na_3Ti_2(PO_4)_3 \rightarrow 2Na^+ + 2e^- + NaTi_2(PO_4)_3$$

During the charging process, the electrode material $NaTi_2(PO_4)_3$ reacts with two sodium ions (Na^+) and two electrons (e^-) from the electrolyte to form $Na_3Ti_2(PO_4)_3$. This reaction enables more sodium ions to intercalate into the material, resulting in a compound with a higher sodium content, thereby storing electrical energy. During the discharge process, the two sodium ions in $Na_3Ti_2(PO_4)_3$ are extracted, and two electrons are released. These sodium ions and electrons flow through the external

circuit, providing current and releasing the stored energy of the battery. After discharge, the material returns to the $NaTi_2(PO_4)_3$ state. The process of sodium ion intercalation during charging stores energy, while extraction during discharging releases energy. This process is reversible, allowing the battery to undergo multiple charge-discharge cycles. Simultaneously, the high electrical conductivity of FeNi carbon-doped materials contributes to an enhanced reaction rate and improved cycling performance of the batteries. Additionally, these materials enhance the conductivity and electron transfer capabilities of NTP, thereby significantly boosting the overall electrochemical performance.

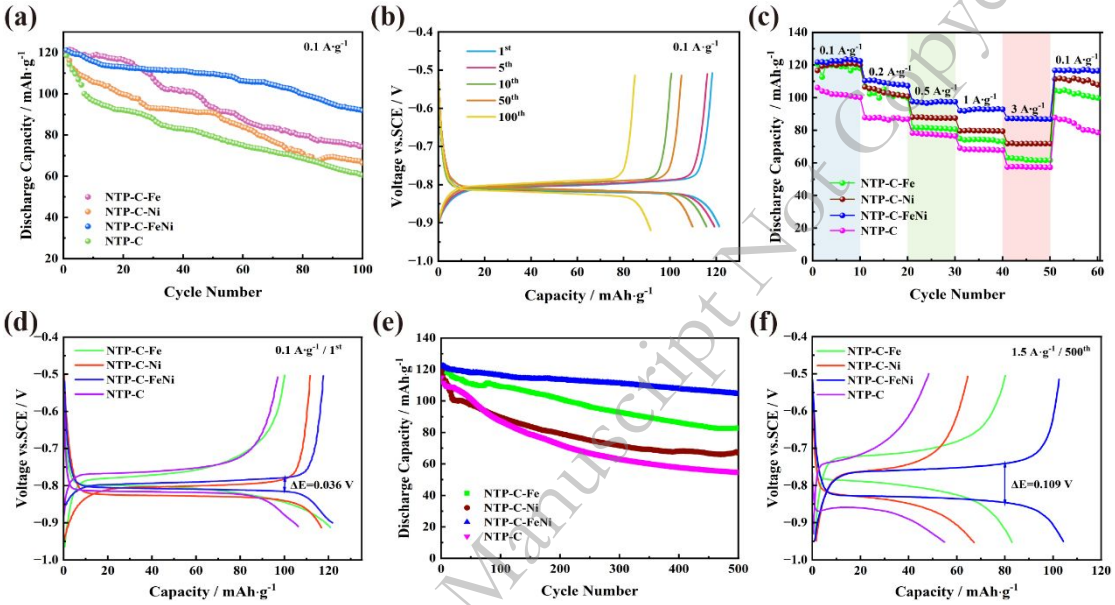

Fig. 6. (a) Cycling performance of NTP-C-Fe, NTP-C-Ni, NTP-C-FeNi and NTP-C at 0.1 A/g; (b) Capacity-voltage curves of NTP-C-FeNi with different cycles at 0.1 $A \cdot g^{-1}$; (c) Rate capability of NTP-C-Fe, NTP-C-Ni, NTP-C-FeNi and NTP-C; (d) Capacity-voltage curves of NTP-C-Fe, NTP-C-Ni, NTP-C-FeNi and NTP-C at 0.1 $A \cdot g^{-1}$ for the first cycle; (e) Long cycle capability of NTP-C-Fe, NTP-C-Ni, NTP-C-FeNi and NTP-C at 1.5 $A \cdot g^{-1}$; (f) Capacity-voltage curves of NTP-C-Fe, NTP-C-Ni, NTP-C-FeNi and NTP-C at 1.5 $A \cdot g^{-1}$ for the 500^{th} cycle.

5.3. Electrochemical behavior of NTP composites

The sodium ion diffusion kinetics of NTP-C-Fe, NTP-C-Ni, and NTP-C-FeNi were evaluated through CV curves at the various scan rates and the linear relationship between the oxidation-reduction peak current and the square root of the scan rate. Figs

7(a) (c) and (e) presents the CV curves of the three composite electrode materials at sweep speeds of 0.2, 0.5, 1, 5, and 10 mV·s^{-1}. It can be found that as the scanning rate increases, the sodium ions on the electrode surface may not migrate in time, leading to increased polarization and a rise in peak potential difference [44]. The CV curves of the three composite materials reflected variations in the corresponding peak currents and redox peak potentials. These variations occurred due to the increase in current response as the scan rate increased. Consequently, at sufficiently high scanning rates, the potential difference between the redox peaks of the materials will be primarily influenced by the scanning rate. Despite slight shifts and gradual broadening of the redox peak pairs as the scanning rate increases, the essential characteristics of the curve remain unchanged, indicating the good electrochemical reversibility of the material. However, NTP-C-FeNi materials exhibit higher current densities, indicating that the electrochemical reaction rate on the surface of the NTP-C-FeNi electrode is higher, resulting in higher capacity and faster kinetics. According to the principles of electrochemical reaction kinetics [45], the relationship between peak current (i) and scan rate (υ) follows a power-law equation:

$$i = a\upsilon^b$$

where a and b are adjustable parameters, and the value of b reflects the nature of the electrochemical response. When b-value is close to 0.5, the electrochemical reaction is controlled by semi-infinite linear diffusion; when the value of b is close to 1, it indicates that the electrochemical reaction is biased towards surface control. From Figs. S5(a-c), it can be concluded that diffusion-controlled intercalation dominates the sodium ion storage in all three composites electrode materials, NTP-C-Fe, NTP-C-Ni, and NTP-C-FeNi.

Due to the similar electrochemical behavior of NTP-C-Fe, NTP-C-Ni, and NTP-C-FeNi at different scan rates, it indicates that they possess rapid reaction kinetics. Subsequently, the sodium ion diffusion coefficients of the three composites materials were calculated from the Randles-Sevcik equation [46]:

$$i_p = 0.4463(F^3/RT)^{1/2} n^{3/2} A D^{1/2} C_0^* v^{1/2}$$

where i_p is the peak current value of the oxidation-reduction peak, F is the Faraday constant, R is the molar gas constant, T is the thermodynamic temperature, n is the number of transferred electrons, A is the area of the electrode, $C_0^*$is the concentration of sodium ion in the NTP solidoid, and υ is the scan speed. C_0^* is calculated using equation:

$$C = \rho / M$$

In the equation, ρ is 2.84 g·cm^{-1}, and M is 404 g·mol^{-1}. The plots of peak current density versus square root of scan rate are shown in Figs. 7(b) (d) and (f) for NTP-C-Fe, NTP-C-Ni, and NTP-C-FeNi, respectively. From which, NTP-C-FeNi composites in ASIB with diffusion coefficients of (D_a = 2.95×10^{-10}) and (D_c = 9.41×10^{-10}), which are superior to NTP-C-Fe and NTP-C-Ni. This indicates that NTP-C-FeNi exhibits rapid diffusion kinetics. This result further confirms that FeNi-C composites can effectively promote the fast mobility of Na^+ in ASIBs, facilitate fast reactions, and thus enhance the sodium storage capacity of NTP.

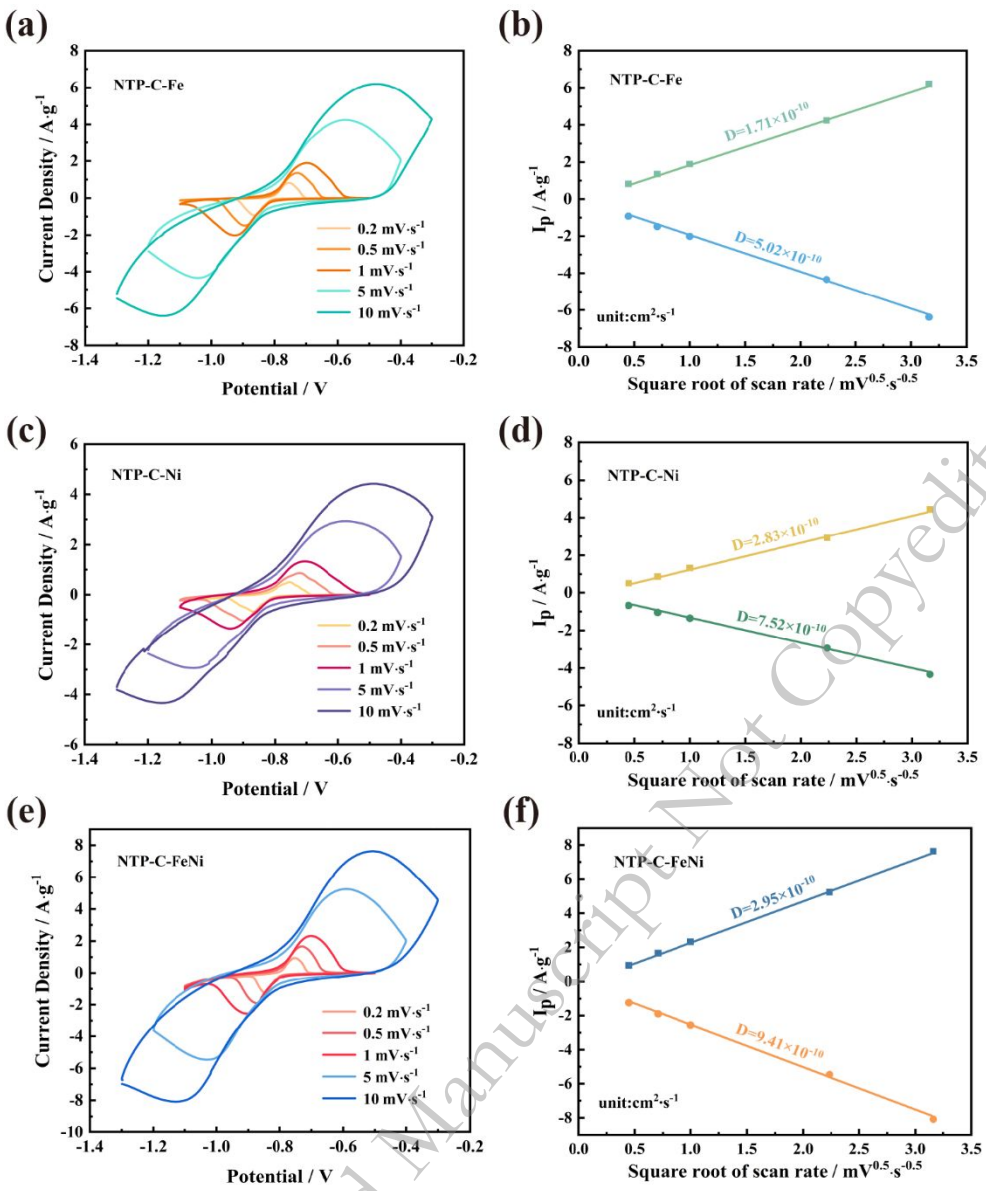

Fig. 7. (a) CV curve of NTP-C-Fe; (b) Correlation between peak current density and square root of scan rate for NTP-C-Fe; (c) CV curve of NTP-C-Ni; (d) Correlation between peak current density and square root of scan rate for NTP-C-Ni; (e) CV curve of NTP-C-FeNi; (f) Correlation between peak current density and square root of scan rate for NTP-C-FeNi.

Figs. 8(a-c) depict the EIS of NTP-C-Fe, NTP-C-Ni, and NTP-C-FeNi composite electrode materials, measured over a frequency range of 0.01 to 10^6 Hz. The corresponding equivalent circuit is provided in Supporting Information Fig. S6. The EIS spectra are characterized by semicircles in the high-frequency region and fitted slopes in the low-frequency region, representing the respective characteristics of these

frequency ranges. The semicircle is caused by charge transfer impedance (R_{ct}), the fitting slope is related to ion diffusion kinetics. The impedance parameters R_s, R_{ct} and Warburg impedance of the ASIB system were calculated by simulating the reactions in the battery using an equivalent circuit and the results are shown in Table S2. NTP-C-FeNi was found to exhibit a smaller R_{ct} and a larger Warburg impedance, indicating lower charge transfer impedance and higher ion diffusion kinetics. These results further confirm that NTP-C-FeNi possesses a good Na^+ diffusion rate, which contributes to its excellent Na^+ storage performance.

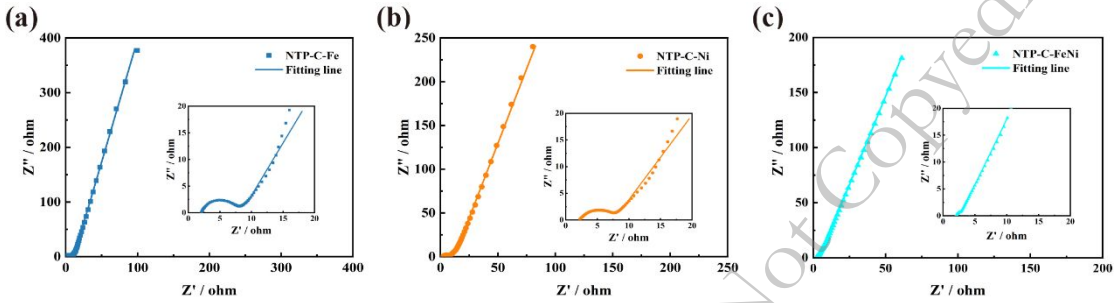

Fig. 8. Electrochemical impedance spectroscopy (a) NTP-C-Fe; (b) NTP-C-Ni; (c) NTP-C-FeNi of the composite.

6. Conclusion

Bimetallic-doped carbon-coated NTP complexes were successfully synthesized by a sol-gel approach, which enhanced structural stability and raised the conductivity of NTP for rapid Na^+ insertion/extraction. Among them, the NTP-C-FeNi composite showed excellent electrochemical performance in ASIBs. The first-cycle discharge capacities were 121.72, 110.42, 97.71, 92.08, and 87.29 $mAh \cdot g^{-1}$ at 0.1, 0.2, 0.5, 1, and 3 $A \cdot g^{-1}$, respectively. After 500 cycles at 1.5 $A \cdot g^{-1}$, the capacity remained at 85.3%. Additionally, the insertion mechanism of Na^+ in NTP-C-Fe, NTP-C-Ni, and NTP-C-FeNi composites was investigated in the three-electrode system, the diffusion kinetics of Na^+ were analyzed. The results show that Na^+ in the NTP-C-FeNi materials have a fast ion migration rate in ASIBs. Therefore, the rate performance and cycling performance of the NTP material were improved after FeNi-C doping. This bimetallic-doped carbon composite NTP material has the benefits of a big specific surface area, stable chemistry, fast Na^+ transfer kinetics, which also provide a

research idea for the application of ASIBs based on NTP anode in field of energy storage.

Acknowledgements

This work is supported by the National Natural Science Foundation of China (52072298, 51802261), Scientific Research Program Funded by Shaanxi Provincial Education Department (Program No.23JK0662), Natural Science Foundation of Shaanxi Province
(2023-JC-YB-515), and the Youth Innovation Team of Shaanxi Universities.

Conflicts of interest

The authors declare that they have no known competing financial interests or personal relationships that could have appeared to influence the work reported in this paper.

References

[1] T. Fujita, H. Chen, K.T. Wang, C.L. He, Y.B. Wang, G. Dodbiba and Y.Z. Wei, Reduction, reuse and recycle of spent Li-ion batteries for automobiles: A review, *International Journal of Minerals, Metallurgy and Materials*, 28 (2021), No.2, p.179-192.

[2] G.Q. Yang, C. Lee, X.X. Qiao, S.K. Babu, U. Martinez and J.S. Spendelow, Advanced electrode structures for proton exchange membrane fuel cells: Current status and path forward, *Electrochemical Energy Reviews*, 7 (2024), No.1, p.9.

[3] M.J. Shi, H.T. Zhu, C. Chen, J.T. Jiang, L.P. Zhao and C. Yan, Synergistically coupling of graphene quantum dots with Zn-intercalated MnO_2 cathode for high-performance aqueous Zn-ion batteries, *International Journal of Minerals, Metallurgy and Materials*, 30 (2023), No.1, p.25-32.

[4] Y. Zhao, B. Wang, M.J. Shi, S.B. An, L.P. Zhao and C. Yan, Mg-intercalation engineering of MnO_2 electrode for high-performance aqueous magnesium-ion batteries, *International Journal of Minerals, Metallurgy and Materials*, 29 (2022), No.11, p.1954-1962.

[5] Y.L. Liang and Y. Yao, Designing modern aqueous batteries, *Nature Reviews Materials*, 8 (2023), No.2, p.109-122.

[6] D.Y. Lan, X.F. Qu, Y.T. Tang, L.Y. Liu and J. Liu, Acetate solutions with 3.9 V electrochemical stability window as an electrolyte for low-cost and high-performance aqueous sodium-ion batteries, *Journal of Electrochemistry*, 28 (2022), No.1, p.6.

[7] B. Li, P.C. Ruan, X.Y. Xu, Z.X. He, X.Y. Zhu, L. Pan, Z.Y. Peng, Y.Y. Liu, P. Zhou and B.G. Lu, Covalent organic framework with 3D ordered channel and multi-functional groups endows Zn anode with superior stability, *Nano-Micro Letters*, 16 (2024), No.1, p.76.

[8] Y. Han, S.Y. Liu, L. Cui, L. Xu, J. Xie, X.K. Xia, W.K. Hao, B. Wang, H. Li and J. Gao, Graphene-immobilized flower-like Ni_3S_2 nanoflakes as a stable binder-free anode material for sodium-ion batteries, *International Journal of Minerals, Metallurgy and Materials*, 25 (2018), No.1, p.88-93.

[9] C.S. Ding, Z. Chen, C.X. Cao, Y. Liu and Y.F. Gao, Advances in Mn-based electrode materials for aqueous sodium-ion batteries, *Nano-Micro Letters*, 15 (2023), No.1, p.192.

[10] W. Li, J.P. Li, R.R. Li, X.L. Li, J. Gao, S.M. Hao and W.D. Zhou, Study on sodium storage properties of manganese-doped sodium vanadium phosphate cathode materials, *Battery Energy*, 2 (2023), No.2, p.20220042.

[11] S.Z. Zhao, H.Y. Che, S.L. Chen, H.X. Tao, J.P. Liao, X.Z. Liao and Z.F. Ma, Research progress on the solid electrolyte of solid-state sodium-ion batteries, *Electrochemical Energy Reviews*, 7 (2024), No.1, p.3.

[12] T. Xu, J.J. Yu, J.C. Ma, W. Ren, M.L. Hu and X.F. Li, The critical role of water molecules in the development of aqueous electrolytes for rechargeable metal-ion batteries, *Journal of Materials Chemistry A*, (2024).

[13] C. Delmas, F. Cherkaoui, A. Nadiri and P. Hagenmuller, A nasicon-type phase as intercalation electrode: $NaTi_2(PO_4)_3$, *Materials research bulletin*, 22 (1987), No.5, p.631-639.

[14] S.I. Park, I. Gocheva, S. Okada and J.-I. Yamaki, Electrochemical properties of $NaTi_2(PO_4)_3$ anode for rechargeable aqueous sodium-ion batteries, *Journal of The Electrochemical Society*, 158 (2011), No.10, p.A1067.

[15] S.Y. Lee, D. Park, B.S. Yoon, Y.-S. Lee, Y.I. Park and C.H. Ko, Atomic layer deposition-based synthesis of TiO_2 and Al_2O_3 thin-film coatings on nanoparticle powders for sodium-ion batteries with enhanced cyclic stability, *Journal of Alloys Compounds*, 897 (2022), p.163113.

[16] W.J. Wang, J.T. Wu and C.L. Zeng, New construction of polypyrrole interphase layers to improve performance stability of $NaTi_2(PO_4)_3$ anode for aqueous Na-ion batteries, *Solid State Ionics*, 397 (2023), p.116259.

[17] L. Birk, K. Rener-Sitar, M. Benčina and I. Junkar, Dental silicate ceramics surface modification by nonthermal plasma: a systematic review, *Dental Materials*, (2024).

[18] X.H. Liu, X.T. Xu, X.X. Xuan, W. Xia, G.L. Feng, S.H. Zhang, Z.G. Wu, B.H. Zhong, X.D. Guo and K.Y. Xie, Unlocking enhanced capacitive deionization of $NaTi_2(PO_4)_3$/carbon materials by the yolk–shell design, *Journal of the American chemical society*, 145 (2023), No.16, p.9242-9253.

[19] D.H. Lu, J.J. Zhang, Z.B.H. Wei and Z.B. Wang, Reducing atmosphere improves the conductivity of $NaTi_2(PO_4)_3$/C material for hybrid aqueous rechargeable lithium-ion battery anode, *Ceramics International*, 48 (2022), No.18, p.26408-26415.

[20] X.H. Qin, Y.H. Du, P.C. Zhang, X.Y. Wang, Q.Q. Lu, A.K. Yang and J.C. Sun, Layered barium vanadate nanobelts for high-performance aqueous zinc-ion batteries, *International Journal of Minerals, Metallurgy and Materials*, 28 (2021), No.10, p.1684-1692.

[21] J.T. Wu, L.X. Yang, H.J. Liu, H.P. Bu, W.J. Wang, C.L. Zeng and S.L. Zhu, Effect of Al doping on electrochemical performance of $NaTi_2(PO_4)_3$/C anode for aqueous sodium ion battery, *Journal of Applied Electrochemistry*, 52 (2022), No.11, p.1563-1572.

[22] X.J. Liu, Z.F. Li, X.H. Zhong, C.X. Wang and S. Dmytro, Dual strategy of La^{3+} doping

and carbon coating enhancing the rate performance of $NaTi_2(PO_4)_3$ anode materials, *Ionics*, 30 (2024), No.3, p.1437-1445.

[23] Z. Tang, S.Y. Zhou, Y.C. Huang, H. Wang, R. Zhang, Q. Wang, D. Sun, Y.G. Tang and H.Y. Wang, Improving the initial coulombic efficiency of carbonaceous materials for Li/Na-ion batteries: origins, solutions, and perspectives, *Electrochemical Energy Reviews*, 6 (2023), No.1, p.8.

[24] T. Xu, M.S. Zhao, Z. Li, Z. Su, W. Ren, S. Yang and V.G. Pol, A high rate and long cycling performance $NaTi_2(PO_4)_3$ core–shell porous nanosphere anode for aqueous sodium-ion batteries, *Energy Technology*, 10 (2022), No.11, p.2200970.

[25] M.L. Lu, T. Li, X.Q. Yang, Y. Liu and X.D. Xiang, A liquid-phase reaction strategy to construct aqueous sodium-Ion batteries anode with enhanced redox reversibility and cycling stability, *Chemical Engineering Science*, 274 (2023), p.118700.

[26] C. Wu, P. Kopold, Y.L. Ding, P.A. Van Aken, J. Maier and Y. Yu, Synthesizing porous $NaTi_2(PO_4)_3$ nanoparticles embedded in 3D graphene networks for high-rate and long cycle-life sodium electrodes, *ACS nano*, 9 (2015), No.6, p.6610-6618.

[27] Y.L. Wu, Q. Zou, C.L. Li and W.H. Wang, Structural reinforced $NaTi_2(PO_4)_3$ composite by pillar effects for constructing a high-performance rocking-chair desalination battery, *Chemical Engineering Journal*, 480 (2024), p.147965.

[28] J.J. Gu, S.J. Zhang, X.Y. Zhang, C.Y. Li, A.H. Wu, Q.H. Li, W.T. Mao and K.Y. Bao, $NaSn_{0.02}Ti_{1.98}(PO_4)_3$/C as a promising anode material with high performance for sodium-ion batteries, *Journal of Solid State Electrochemistry*, (2023), p.1-9.

[29] S. Difi, I. Saadoune, M.T. Sougrati, R. Hakkou, K. Edstrom and P.-E. Lippens, Role of iron in $Na_{1.5}Fe_{0.5}Ti_{1.5}(PO_4)_3$/C as electrode material for Na-ion batteries studied by operando Mössbauer spectroscopy, *Hyperfine Interactions*, 237 (2016), p.1-9.

[30] J.T. Wu, H.J. Liu, H.P. Bu, X. Zhang, H.L. Zhang, W.J. Wang, L.X. Yang, C.L. Zeng and S.L. Zhu, Manganese-based NASICON structured $Na_{1+2x}Mn_xTi_{2-x}(PO_4)_3$ as promising cathode in aqueous sodium ion battery, *Journal of Alloys Compounds*, 934 (2023), p.167872.

[31] Y.K. Xi, X.X. Wang, H. Wang, M.J. Wang, G.J. Wang, J.Q. Peng, N.J. Hou, X. Huang, Y.Y. Cao and Z.H. Yang, Optimizing the electron spin states of $Na_4Fe_3(PO_4)_2P_2O_7$ cathodes via Mn/F dual-doping for enhanced sodium storage, *Advanced Functional Materials*, 34 (2024), No.16, p.2309701.

[32] P. Wei, Y.X. Liu, Y.R. Su, L. Miao, Y.Y. Huang, Y. Liu, Y.G. Qiu, Y.Y. Li, X.Y. Zhang and Y. Xu, F-doped $NaTi_2(PO_4)_3$/C nanocomposite as a high-performance anode for sodium-ion batteries, *ACS applied materials interfaces*, 11 (2018), No.3, p.3116-3124.

[33] Q.C. Wang, S. He, H. Chen, Z.Q. Peng, Z.X. Xu, Z.Y. Zeng, C. Wang, P. Xue, L.B. Ni and X.G. Li, Tailoring the electronic structure of the $NaTi_2(PO_4)_3$ anode for high-performing sodium-ion batteries via defect engineering, *Green Chemistry*, 26 (2024), No.4, p.2114-2123.

[34] B. He, K.B. Yin, W.B. Gong, Y.W. Xiong, Q.C. Zhang, J. Yang, Z.X. Wang, Z. Wang, M.X. Chen and P. Man, $NaTi_2(PO_4)_3$ hollow nanoparticles encapsulated in carbon nanofibers as novel anodes for flexible aqueous rechargeable sodium-ion batteries, *Nano Energy*, 82 (2021), p.105764.

[35] A. Mukherjee, S. Banerjee and S.B. Majumder, Improvement of sodium storage

performance of N-doped carbon coated $NaTi_2(PO_4)_3$ derived from polyvinyl pyrrolidone, *Journal of Materials Science: Materials in Electronics*, 34 (2023), No.21, p.1602.

[36] J.R. He and A. Manthiram, 3D CoSe@C aerogel as a host for dendrite-free lithium-metal anode and efficient sulfur cathode in Li–S full cells, *Advanced Energy Materials*, 10 (2020), No.41, p.2002654.

[37] J. Qin, T.S. Wang, D.Y. Liu, E.Z. Liu, N.Q. Zhao, C.S. Shi, F. He, L.Y. Ma and C.N. He, A top-down strategy toward SnSb in-plane nanoconfined 3D N-doped porous graphene composite microspheres for high performance Na-ion battery anode, *Advanced Materials*, 30 (2018), No.9, p.1704670.

[38] W.N. Ren, W.J. Zang, H.F. Zhang, J.L. Bian, Z.F. Chen, C. Guan and C.W. Cheng, PtCo bimetallic nanoparticles encapsulated in N-doped carbon nanorod arrays for efficient electrocatalysis, *Carbon*, 142 (2019), p.206-216.

[39] Y. Liu, X. Liu, X.Y. Wang, S. Ullah, Y. Peng, G.Y. Pan, W.J. Gao, B.Y. Song, X.H. Zhang and A. Jia, Synergistic bimetallic effects of BiSb anodes enable long-stable sodium storage, *Advanced Functional Materials*, (2024), p.2415092.

[40] K.Z. Cao, J.H. Ma, Y.L. Dong, Y. Duan, R.T. Zheng, D. Bundhooa, H.Q. Liu and Y. Lei, Graphitic carbons: preparation, characterization, and application on K-ion batteries, *Rare Metals*, 43 (2024), p.4056-4075.

[41] J.B. Li, Z.Q. Li, S.C. Tang, T.Y. Wang, K. Wang, L.K. Pan and C.Y. Wang, Sodium titanium phosphate nanocube decorated on tablet-like carbon for robust sodium storage performance at low temperature, *Journal of Colloid Interface Science*, 629 (2023), p.121-132.

[42] X. Liu, M.L. Zhang, X.Y. Wang, Y. Peng, Y. Liu, S. Ullah, Z.H. Duan, W.J. Gao, B.Y. Song and M.X. Wei, Evidence of quasi-na metallic clusters in sodium ion batteries through in situ X-Ray diffraction, *Advanced Materials*, (2024), p.2410673.

[43] G. Plečkaitytė, M. Petrulevičienė, L. Staišiūnas, D. Tediashvili, J. Pilipavičius, J. Juodkazytė and L. Vilčiauskas, Understanding and mitigation of $NaTi_2(PO_4)_3$ degradation in aqueous Na-ion batteries, *Journal of Materials Chemistry A*, 9 (2021), No.21, p.12670-12683.

[44] B. Luo, W.G. Wang, Q. Wang, W.J. Ji, G.H. Yu, Z.H. Liu, Z.W. Zhao, X.W. Wang, S.B. Wang and J.F. Zhang, Facilitating ionic conductivity and interfacial stability via oxygen vacancies-enriched TiO_2 microrods for composite polymer electrolytes, *Chemical Engineering Journal*, 460 (2023), p.141329.

[45] H. Gao, W.L. Gao and M. Pumera, 3D-printed nanostructured copper substrate boosts the sodiated capability and stability of antimony anode for sodium-ion batteries, *Advanced Functional Materials*, 34 (2024), No.19, p.2310563.

[46] R.F. Ubbink, S. Gudjonsdottir, Y.B. Vogel and A.J. Houtepen, Numerical model to simulate electrochemical charging of nanocrystal films, *The Journal of Physical Chemistry C*, 127 (2023), No.20, p.9896-9902.